

Unravelling the Mechanics of Knitted Fabrics Through Hierarchical Geometric Representation

Xiaoxiao Ding^{a,b}, Vanessa Sanchez^{a,c}, Katia Bertoldi^a, Chris H. Rycroft^{b,d}

^a*Harvard John A. Paulson School of Engineering and Applied Sciences, Harvard University, Cambridge, MA 02138, USA,*

^b*Department of Mathematics, University of Wisconsin–Madison, Madison, WI 53706, USA,*

^c*Department of Chemical Engineering, Stanford University, 443 Via Ortega, Stanford, CA 94305, USA,*

^d*Computational Research Division, Lawrence Berkeley Laboratory, 1 Cyclotron Road, Berkeley, CA 94720, USA,*

Abstract

Knitting interloops one-dimensional yarns into three-dimensional fabrics that exhibit behaviours beyond their constitutive materials. How extensibility and anisotropy emerge from the hierarchical organization of yarns into knitted fabrics has long been unresolved. We sought to unravel the mechanical roles of tensile mechanics, assembly and dynamics arising from the yarn level on fabric nonlinearity by developing a yarn-based dynamical model. This physically validated model captures the fundamental mechanical response of knitted fabrics, analogous to flexible metamaterials and biological fiber networks due to geometric nonlinearity within such hierarchical systems. We identify the dictating factors of the mechanics of knitted fabrics, highlighting the previously overlooked but critical effect of pre-tension. Fabric anisotropy originates from observed yarn–yarn rearrangements during alignment dynamics and is topology-dependent. This yarn-based model also provides design flexibility of knitted fabrics to embed functionalities by allowing variation in both geometric configuration and material property. Our hierarchical approach to build up a knitted fabrics computationally modernizes an ancient craft and represents a first step towards mechanical programmability of knitted fabrics in wide engineering applications.

Email addresses: xiaoxiaoding@g.harvard.edu (Xiaoxiao Ding),
chr@math.wisc.edu (Chris H. Rycroft)

Preprint submitted

July 25, 2023

1. Introduction

Knitted fabrics are hierarchical structures that build up from microscale to macroscale, as yarns are the primary building blocks to dominate the physics and design of fabrics. The separation of these two scales (i.e., yarn-level and fabric-level) at the structural level (mesoscale) not only causes a range of interesting physical phenomena [1, 2] to arise, but also provides a huge design space for functionalities in knitted fabrics beyond what their constitutive materials can achieve. Knitted fabrics represent nonbiological examples of a nonlinear elastic response characterised by a “J-shape” curve, as the fabric transitions from bending energy dominant region to stretching energy dominant region under uniaxial tension. The presence of fabric patterns at the mesoscale allows the whole fabric to take sustainable tensile stress under low strains on the individual yarn segments, as yarn alignment dynamics provide geometric degrees of freedom for fabric. The distinctively compliant behaviour of knitted fabrics makes them stand out as excellent scaffolds for soft robotic actuators [3, 4, 5], responsive wearable devices [6, 7] and in vivo health monitoring devices [8], where large deformation and flexible morphing without material damage is desired. The anisotropy at the fabric mesoscale can be exploited to fine tune actuation of such devices [9], where carefully selected structures can be spatially varied across the fabric, to generate morphing that provides customised fit to complex geometries. Multifunctional knitted fabrics can be created through embedding functional yarns into conventional knit structures, to further enlarge the design space of knitted fabrics to mimic morphing biological structures [10] and to serve as light and touch sensors [5], pressure sensors [11], electronic interfaces [12] and electronic skins [13] for an unravelling future of human machine interaction.

Currently, intuition-led strategies remain the primary approach to design devices made of knitted fabrics. This paradigm poses limitations on exploring the design space due to high machinery costs, training costs and material waste. A generalisation of these application-driven designs for yarn geometries, fabric structures and material variations has not yet been established. Early theoretical work on knitted structures hypothesise that the fabric shape is predominantly determined by the geometric description of knit structure rather than constitutive material. Starting from a three-dimensional parameterisation of the jersey knit pattern [14] to curvature augmented model [15], followed

by energy minimisation model [16], most geometric models of knitted fabrics are constructed through superposition of cosine and sine curves due to the smoothness and periodicity of these shape functions. With the development of spline basis functions, we can discretise yarns with sufficient accuracy and such yarn-based models [17, 18, 19, 20] stand out compared to coarse-grained models [21, 22, 23, 24] and homogenised models [25, 26, 27, 28, 29, 30, 31], due to their capability to (i) capture mechanical behavior originating from first principles via yarn dynamics, (ii) provide quantitative measurements of geometric nonlinearities arising across scales, and (iii) integrate multiple fabric structures within complex 3D configurations, all while maintaining unconstrained extensibility of individual yarns.

In this work, we detail the development and implementation of a mechanics-centered computational model of knitted fabrics, as a step towards mechanical programmability of textile-based metamaterials. To begin, we adopt a yarn-based model with cubic order spline basis functions [18] that was originally applied in computer graphics to animate cloth in a qualitatively realistic manner. We are the first to extend and validate this model against machine knitted fabrics at full scale, to provide physical insights into across-scale mechanical behaviours. Our numerical approach is implemented through fully dynamic formulation of the governing equation of motion, integrated explicitly with an adaptive scheme. A key aspect of our numerical procedure is the introduction of relaxation stage before the application of external tensile forces, to account for residue stresses that are inherent in the knit fabrication process. This residue stress typically poses a challenge in generating an accurate ground truth reference state from purely the geometric description of knitted fabrics, and are lacking in existing work. We treat the dynamics at a continuous yarn as the governing mechanics, and connect yarns through translation and interpolation to form fabrics. On one hand, this approach enables the prediction of local, spatial evolution of bending and stretching energy, echoing a broader interest in how soft materials gradually adapt to applied elastic energy. As we can directly compute measurements of energy, stretch and alignment with regard to each yarn segment, we can predict micromechanical hot spots. Moreover, this model enables the interactive design of complex fabric configurations, which possess inhomogeneous mechanical fields through varying fabric structures or material properties. We can further fine tune fabric configurations with mechanical insights gained from micromechanical lenses, as we leverage the advantages of the hierarchical geometric representation.

In addition to providing quantitatively calibrated physical results and

motivating examples for more detailed study, we show evidence that structural properties, such as varying topological description of fabric patterns [32] and varying spatial distribution of fabric patterns can effectively adjust the mechanical behaviour of knitted fabrics, without modifying the material properties. Moreover, we discuss the potential for using our model to further extend the design space from basic knitted fabric structures, leading towards a programmable future of functional textiles.

2. Theoretical background

2.1. Discretisation of the yarn, and initial conditions for the fabric

Our work builds on previous yarn-level simulations by Kaldor et al. [18] that were originally developed in the computer graphics literature. We implemented a custom code in C++, using OpenMP for multithreading, to perform the simulations. In this section we provide a mathematical overview of the methods, and then provide additional technical and computational details in Section 5.1.

Our simulation can handle an arbitrary number of individual yarns of diameter d . The centerline of each yarn is represented by a cubic B-spline with N segments. We denote $s \in \Omega = [0, N]$ to be a dimensionless coordinate along the yarn, where the $N + 1$ control points of the spline are located at $s = 0, 1, 2, \dots, N$. The cubic B-spline basis function is given by

$$B(s) = \begin{cases} \frac{2}{3} - s^2 + \frac{1}{2}|s|^3 & \text{if } |s| < 1, \\ \frac{1}{6}||s| - 2|^2 & \text{if } 1 \leq |s| < 2, \\ 0 & \text{otherwise.} \end{cases} \quad (1)$$

A family of basis functions is then given by $b_k(s) = B(s - k)$ for $k \in \mathbb{Z}$. The yarn is then defined as

$$\mathbf{y}(s, t) = \sum_{k=-1}^{N+1} b_k(s) \mathbf{q}_k(t), \quad (2)$$

where $\mathbf{q}_k(t)$ are time-dependent three-dimensional functions. In Eq. (2), the sum must run from -1 to $N + 1$ in order to describe all piecewise cubics in $C^2[0, N]$ [33], making for $m = N + 3$ terms in total. Hence, the

yarn is described by $3m = 3(N + 3)$ degrees of freedom stored in a vector $\mathbf{q} = (\mathbf{q}_{-1}, \mathbf{q}_0, \dots, \mathbf{q}_{N+1})$. The velocity of the yarn is given by

$$\mathbf{v}(s, t) = \dot{\mathbf{y}}(s, t) = \sum_{k=-1}^{N+1} b_k(s) \dot{\mathbf{q}}_k(t), \quad (3)$$

where a dot represents a derivative with respect to t . The velocity of the yarn is analogously described by a $3m$ -component vector $\dot{\mathbf{q}}$. The descriptions in Eqs. (2) & (3) effectively decouple the spatial and temporal dependence of the yarn motion. In its rest state, the yarn has equal arc length l between each pair of control points.

We initialize the spline at $t = 0$ by specifying an initial parametric curve for its shape. In our work, we primarily focus on simulating knitted fabrics that are generated from loop units that are formed stitch by stitch in the weft (horizontal) and warp (vertical) directions. Depending on the direction along which a continuous yarn is fed in, knitted fabrics fall into two categories, weft knits and warp knits. We focus on weft-knitted fabrics in this work, as they are compatible to standardised samples made from commercially available V-bed knitting machines.

A typical loop geometry that we employ is [34]

$$\mathbf{y}_p(w) = \begin{pmatrix} \lambda_x \left(w + \sin(\pi w) \right) \\ \lambda_y \cos\left(\frac{\pi w}{2}\right) \\ \lambda_z \cos(\pi w) \end{pmatrix} \quad (4)$$

where $\lambda_x, \lambda_y, \lambda_z$ are scaling parameters in each dimension that may vary independently to match target aspect ratio of generated samples. Using the coordinate range $w \in [w_{\text{start}}, w_{\text{end}}] = [-\frac{\pi}{2}, \frac{\pi}{2}]$ in Eq. (4) yields a single loop as shown in Fig. 2(A). In general, $\|\mathbf{dy}_p/dw\|$ will not be constant, so that the arc length along each parametric curve will not increase at a constant rate in w . Therefore, to initialize the B-spline formulation, our simulation computes the arc length along the curve as a function of w ,

$$A(w) = \int_{w_{\text{start}}}^w \left| \frac{d\mathbf{y}_p}{dw} \right| dw, \quad (5)$$

which is evaluated using composite Gaussian quadrature. The rest arc length is computed as $l = A(w_{\text{end}})/N$. Using the Ridders root-finding method, a

sequence of values $w_0 = w_{\text{start}}, w_1, w_2, \dots, w_N = w_{\text{end}}$ are found such that $A(w_k) = kl$. These set the values of the control points in the B-spline basis formulation, so that $\mathbf{y}(k, 0) = \mathbf{y}_p(w_k)$, giving $N + 1$ vector equations in total. In addition, the direction of the spline at $s = 0, N$ is chosen to match the direction of the parametric curve, giving an additional two vector equations. This gives a total of $N + 3$ linear vector equations that can be solved as a linear system to determine the $\mathbf{q}_k(0)$.

2.2. Dynamics of a yarn

We consider the Lagrangian formulation to describe the dynamics of a single yarn with m control points as

$$\frac{d}{dt} (\nabla_{\dot{\mathbf{q}}} T) - \nabla_{\mathbf{q}} V + \nabla_{\dot{\mathbf{q}}} D = 0, \quad (6)$$

where T is the kinetic energy, V is the potential energy and D is the damping energy. The kinetic energy of the yarn is

$$T(\dot{\mathbf{q}}) = \frac{\rho l}{2} \int_{\Omega} \mathbf{v}^T \mathbf{v} ds, \quad (7)$$

where ρ is the mass density. By referencing Eq. (6), we must evaluate

$$\nabla_{\dot{\mathbf{q}}} T = \rho l \int_{\Omega} (\nabla_{\dot{\mathbf{q}}} \mathbf{v}^T) \mathbf{v} ds. \quad (8)$$

We define the unit mass matrix $M \in \mathbb{R}^{m \times m}$ with components

$$M_{kj} = \int_{\Omega} b_k(s) b_j(s) ds, \quad (9)$$

which corresponds to integrating a product of two B-spline basis functions b_k and b_j . Since each basis function is non-zero over four intervals, $M_{kj} = 0$ if $|k - j| > 3$, and therefore M is a banded matrix with three superdiagonals and three subdiagonals. It remains constant throughout the simulation and can be precomputed. Therefore Eq. (8) becomes

$$\frac{d}{dt} (\nabla_{\dot{\mathbf{q}}} T) = \rho l \sum_{k=-1}^{N+1} M_{jk} \ddot{\mathbf{q}}_j. \quad (10)$$

The potential energy of a yarn includes several terms as

$$V = V^s(\mathbf{q}) + V^b(\mathbf{q}) + V^g(\mathbf{q}), \quad (11)$$

representing energy due to stretching, bending, and gravity. With the assumption of linear elasticity, the stretching energy is given by

$$V^s(\mathbf{q}) = \frac{E^s A l}{2} \int_{\Omega} \left(\frac{\|\mathbf{y}'\|}{l} - 1 \right)^2 ds, \quad (12)$$

where E^s is the tensile stiffness and $A = \pi d^2/4$ is the yarn cross-sectional area. Here, the prime superscript represents a partial derivative with respect to s . The elastic energy of the yarn due to bending is formulated as

$$V^b(\mathbf{q}) = \frac{E^b I l}{2} \int_{\Omega} \kappa^2 ds, \quad (13)$$

where E^b is the bending stiffness, I represents moment of inertia of the yarn cross-section, and the local curvature κ is defined as

$$\kappa = \frac{\|\mathbf{y}' \times \mathbf{y}''\|}{\|\mathbf{y}'\|^3}. \quad (14)$$

The gravitational potential energy is

$$V^g(\mathbf{q}) = \rho l \int_{\Omega} \mathbf{y}^\top \mathbf{g} ds, \quad (15)$$

where \mathbf{g} is the gravitational acceleration. By referencing Eq. (6), we need to evaluate $\nabla_{\mathbf{q}_k} V^s(\mathbf{q})$, $\nabla_{\mathbf{q}_k} V^b(\mathbf{q})$, and $\nabla_{\mathbf{q}_k} V^g(\mathbf{q})$. Similar to evaluating Eq. (10), part of these complicated integrals can be precomputed and the rest can be accurately determined using quadrature.

The damping energy in Eq. (6) has several components. One component is given by

$$D^{\text{iso}}(\dot{\mathbf{q}}) = k_g \int_{\Omega} \mathbf{v}^\top \mathbf{v} ds, \quad (16)$$

which creates a global drag force on the yarns. In the experiments, the knitted samples are primarily in a regime where the forces are in quasi-static equilibrium, since the yarns have sufficient internal damping to remove any transient inertial effects. The drag force in Eq. (16) serves as a simple proxy for the internal damping and accomplishes the same goal, ensuring that the inertial effects are removed.

2.3. Yarn–yarn interactions

The contact forces between two yarns (or between two different sections of the same yarn) are critically important for simulating the knitted fabric. Without loss of generality, let s and \tilde{s} be coordinates ranging from 0 to 1 over two spline segments i and j with a contact. The energy contribution is given by

$$V_{i,j}^{\text{con}} = l^2 \int_0^1 \int_0^1 f \left(\frac{\|\mathbf{y}_i(\tilde{s}) - \mathbf{y}_j(s)\|}{d} \right) ds d\tilde{s}, \quad (17)$$

where \mathbf{y}_i and \mathbf{y}_j are the spline positions on the two segments, and

$$f(\delta) = \begin{cases} k(\delta - 1)^2 & \text{if } 0 \leq \delta < 1, \\ 0 & \text{if } \delta \geq 1, \end{cases} \quad (18)$$

where k is a spring constant. In addition a damping term can be incorporated, with the form

$$D_{i,j}^{\text{fri}} = l^2 \int_0^1 \int_0^1 I(s, \tilde{s}) \left(k_{dt} \|\Delta \mathbf{v}_{ij}\|^2 - (k_{dt} - k_{dn})(\hat{\mathbf{n}}_{ij}^\top \Delta \mathbf{v}_{ij})^2 \right) ds d\tilde{s}, \quad (19)$$

which approximates the effect of frictional sliding. Here $\Delta \mathbf{v}_{ij}$ is the relative velocity and $\hat{\mathbf{n}}_{ij}$ is a normal vector in the collision direction. $I(s, \tilde{s})$ is an indicator function, set to one if $\|\mathbf{y}_i(\tilde{s}) - \mathbf{y}_j(s)\| > d$, and zero otherwise. The constants k_{dt} and k_{dn} set the size of the effect in the tangential and normal directions, respectively.

Unlike the integrals considered in the previous section, it is difficult to evaluate the integrals in Eqs. (17) & (19) efficiently and accurately. Since the integrands are non-smooth, and are only non-zero in localised patches in the (s, \tilde{s}) space, Gaussian quadrature will often give imprecise results. Because of this, we replace each integral with sum over n discrete values $\{s_1, s_2, \dots, s_n\}$ and $\{\tilde{s}_1, \tilde{s}_2, \dots, \tilde{s}_n\}$ so that

$$V_{i,j}^{\text{con}} = l^2 \sum_{\alpha=1}^n \sum_{\beta=1}^n f \left(\frac{\|\mathbf{y}_i(s_\alpha) - \mathbf{y}_j(\tilde{s}_\beta)\|}{d_{\text{con}}} \right), \quad (20)$$

where $s_\alpha = (2\alpha - 1)/n$ and $\tilde{s}_\beta = (2\beta - 1)/n$. This is equivalent to modeling contact between a discrete set of spheres, evenly distributed along each spline segment. Similarly, Eq. (19) is replaced with

$$D_{i,j}^{\text{fri}} = l^2 \sum_{\alpha=1}^n \sum_{\beta=1}^n I_{\alpha\beta} \left(k_{dt} \|\Delta \mathbf{v}_{\alpha\beta}\|^2 - (k_{dt} - k_{dn})(\hat{\mathbf{n}}_{\alpha\beta}^\top \Delta \mathbf{v}_{\alpha\beta})^2 \right), \quad (21)$$

where $\Delta \mathbf{v}_{\alpha\beta} = \mathbf{v}_i(s_\alpha) - \mathbf{v}_j(\tilde{s}_\beta)$ and $\hat{\mathbf{n}}_{\alpha\beta}$ is a normal vector pointing in the direction of $\mathbf{y}_i(s_\alpha) - \mathbf{y}_j(s_\beta)$. $I_{\alpha\beta}$ is set to one if the two spheres are in contact and set to zero otherwise. The diameter d_{con} of the contact spheres is chosen to be slightly larger than the yarn diameter d , so that the envelope made by the spheres more precisely matches the profile of the yarn—see Sec. 5.3 for more information.

To detect the adjacent spheres efficiently, the spheres are binned into an equally-spaced rectangular grid that covers all of the yarns in the simulation. For a given sphere, finding adjacent spheres is performed by iterating over all spheres in nearby grid boxes, resulting in a constant, $O(1)$ computation time per sphere. Even with this optimisation, we typically find that detecting and computing the contact forces is the most computationally expensive step of our simulations.

2.4. Loop topology and fabric pattern

A typical V-bed knitting machine consists of front and back beds that are connected by a carriage to move across the beds and actuate knitting needles positioned along each bed. After yarn carriers feed yarns horizontally to arrays of needles on the knitting beds, the machine actuates the needles by driving the carriage along rows of the knitted fabric and across beds (along columns of the knitted fabric), in order to operate knit (driving a previous loop from front to back) and purl (driving a previous loop from back to front) instructions stitch by stitch. Based on these two basic manufacturing instructions, we can define a set of four representative weft-knit structures as shown in Fig. 1 (A) jersey (all knits or purls), (B) garter 1 by 1 (knits and purls alternating every row only), (C) rib 1 by 1 (knits and purls alternating every column only) and (D) seed 1 by 1 (knits and purls alternating every row and column).

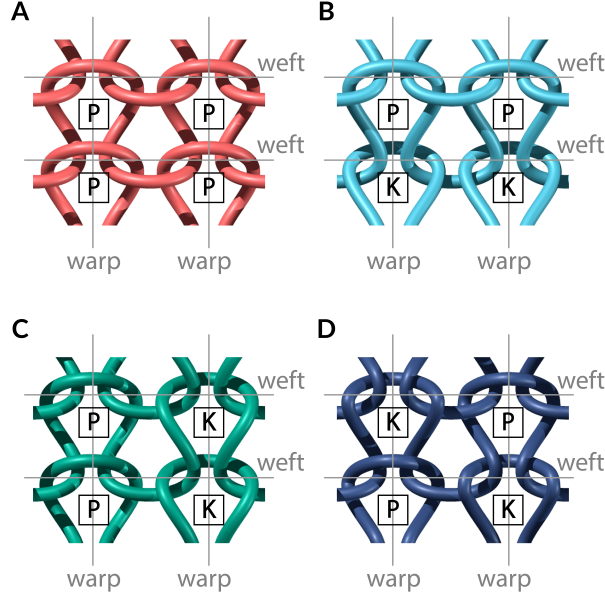


Figure 1: Illustration of basic weft-knitted fabric patterns composed of two by two contacts with varying topology (each contact can either be purl (P) or knit (K) in textile terminology). (A) Jersey, with consistent topology at each contact (all purl or all knit are treated the same due to symmetry in topology). (B) Garter 1 by 1, with contact topology varying row by row. (C) Rib 1 by 1, with contact topology varying column by column. (D) Seed 1 by 1, with contact topology varying every row and column simultaneously.

To be consistent with the manufacturing process [35, 36], we propose a simple pipeline to assemble full-scale weft-knitted fabrics here. Figure 2 illustrates the process of creating a geometric model for jersey, the simplest weft-knitted fabric, since the topology of all contacts within the fabric is consistent. After generating a loop unit along the standardised parametric function, we assemble a row of loops by assigning the end positions of the row along the x axis, similar to how rows of stitches are formed along horizontal needle beds on the V-bed knitting machine. Secondly, we translate each row along the y axis with assigned distance from the central axis of the pattern. Note that modifications to the geometric model are required to adjust for spacing between alternating rows and/or columns in order to create more complex configurations beyond the jersey. We proposed using additional sinusoid function to parameterise the z direction in Eq. (4), in order to alternate wavelength and apply phase shift to accommodate for varying topology [32]. In addition, we specify smooth spiral curves adopting a

generalised helicoid surface [37, 38] equivalent to extra yarns used to cast on and bind off the fabric at the top and bottom boundaries in manufacturing, in order to prevent fabric from unravelling upon free boundary conditions. These spiral curves can be described by

$$\mathbf{y}_s(w) = \begin{pmatrix} \lambda_{x_{\text{spiral}}}(0.25w) \\ \lambda_{y_{\text{spiral}}} \sin(\gamma\pi(w+d)) \\ \lambda_{z_{\text{spiral}}}(1 - \cos(0.5\pi(w+d))) \end{pmatrix}, \quad (22)$$

where $\lambda_{x_{\text{spiral}}}$, $\lambda_{y_{\text{spiral}}}$ and $\lambda_{z_{\text{spiral}}}$ being scaling factors carefully selected to produce tight spirals in order to minimise boundary effects, $\gamma = 0.5$ for patterns with no variation in contact topology with respect to alternating columns (jersey and garter), $\gamma = 0.25$ for patterns with variation in contact topology with alternating columns (rib and seed) and d being the assigned translation distance between rows. It should not exceed the upper bound in order to ensure all rows are attached in initial configuration. Finally, we connect all loose ends of yarns using Hermite interpolation to form a complete fabric solely composed of one continuous yarn.

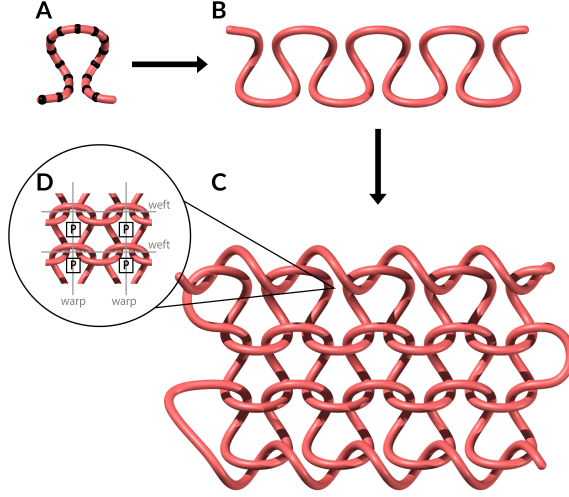


Figure 2: The assembly of a representative weft-knitted fabric (jersey). (A) At the microscale: a loop discretised with evenly spaced control points along fixed cubic basis functions. (B) At the mesoscale: each row of yarn formed and translated based on the topological description of representative structure. We present jersey as an example here and the same assembly process is generalised for other patterns, such as garter, rib and seed. (C) At the macroscale: a fabric with ends of each row connected and additional spiral yarns attached to the top (“casting on” in textile terminology) and bottom boundary (“binding off” in textile terminology) to prevent fabric from unravelling.

2.5. Mechanics-centered simulation framework

After generating knitted fabrics from previously described geometric model, we performed material characterisation tests to calibrate physical parameters relevant to the simulation summarised in Table 1. We then apply loading through tethered springs at sufficiently low loading rate that is critically damped to ensure numerical stability and convergence. We use fourth-order Runge-Kutta integration scheme with adaptive time step. The custom code is implemented in C++ and multithreaded using OpenMP [39].

Table 1: Calibration of physical parameters relevant to the simulation of knitted fabrics.

Symbol	Parameter	Measurement	Dimension in simulation
ρ	mass per unit length	0.077 g/m	7.7×10^{-4} g/cm
l	unit length per stitch	7.23 mm	0.723 cm
r	yarn radius	524 μ m	0.0524 cm
A	yarn cross-sectional area	$A = \pi r^2$	8.63×10^{-3} cm ²
I	yarn moment of inertia	$I = \pi r^4 / 4$	5.92×10^{-6} cm ⁴
E^s	yarn tensile stiffness	79.0 MPa	7.9×10^8 g/(cm s ²)
E^b	yarn bending stiffness	0.249 MPa	2.49×10^4 g/(cm s ²)

3. Results

3.1. Effect of pre-tension on validation

Experimental evidence show that despite specifying the same stitch numbers along both warp and weft directions, the samples made from varying fabric patterns consist of varying dimensions. Typically, yarns within a fabric exhibit residual tension from fabrication process as they are prestressed to be straight and tight when they are fed into the carriers. Hence, it is crucial to capture an accurate reference state configuration of knitted fabric under certain pretension, in order to provide a meaningful comparison between numerical test and experimental test. Since it is hard to obtain the tension a priori, it is hard to establish a relationship between stitch numbers and fabric tightness analytically. Though Eltahan et al. [40] attempted to find this relationship empirically, the results are constrained by the limited dataset on a single jersey pattern. We instead propose to simulate the process of fabrics being prestressed, hence not posing any constraint on the fabric structure nor the material. By using the aspect ratio and unit arclength of simulated samples to benchmark against manufactured samples, we were able to obtain close to ground-truth configurations of all four basic weft-knitted fabrics in their reference states. During the simulation of applying pretension, we enable the fabric to relax to an equilibrium state, as we pull the ends of the continuous yarn closer in a purse-string contraction mechanism. By doing so, we allow the fabric to approach its state that naturally minimises the total bending energy and becomes tighter in configuration.

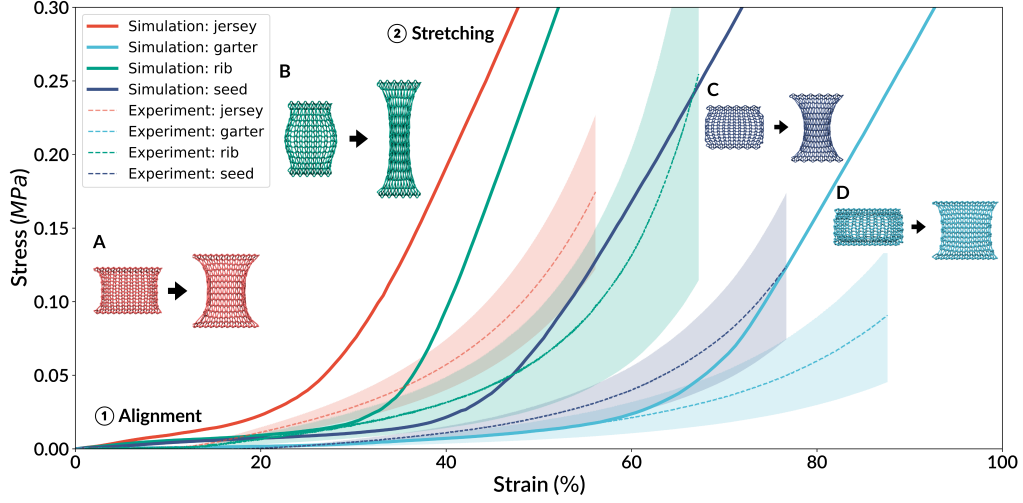


Figure 3: Stress-strain responses measured from simulation and experiment, and simulation snapshots at 20 % strain and 80 % strain for four weft-knitted fabrics (A) jersey, (B) rib 1 by 1, (C) seed 1 by 1 and (D) garter 1 by 1) when subjected to uniaxial tension along warp direction.

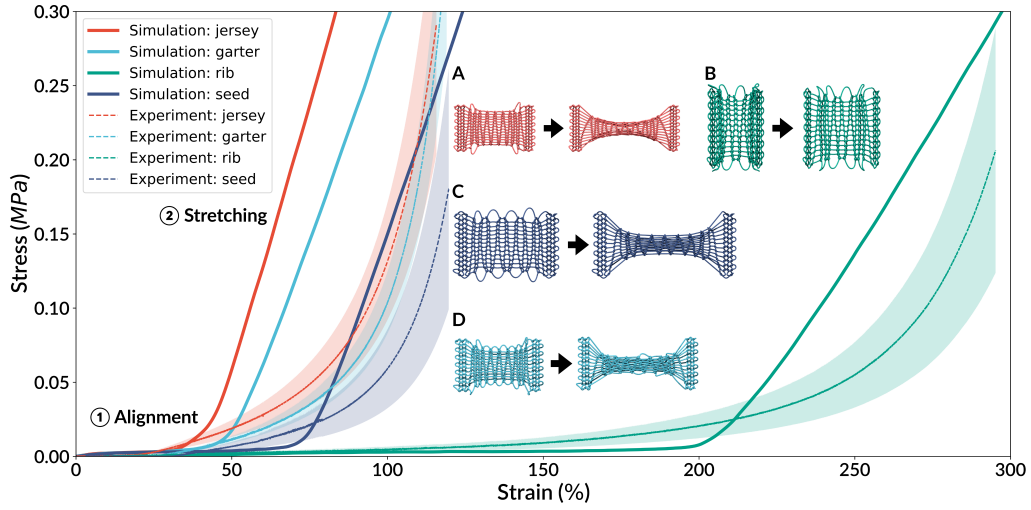


Figure 4: Stress-strain responses measured from simulation and experiment, and simulation snapshots at SI20% strain and 80 % strain for four weft-knitted fabrics (A) jersey, (B) rib 1 by 1, (C) seed 1 by 1 and (D) garter 1 by 1) when subjected to uniaxial tension along weft direction.

3.2. The fundamental mechanical behaviour of knitted fabrics

The influence of geometric flexibility of fabric pattern on the fundamental mechanical response of knitted fabrics is well captured by our numerical model and highlighted in Fig. 3 and Fig. 4, which show applied uniaxial tensile stress σ against strain ϵ in warp and weft directions respectively and the corresponding measurements validated by experiments. To offset variation in fabric dimension S_R along the face formed with yarn diameter $2r$, where the load is applied on, we define tensile stress $\sigma = \frac{F}{2rS_R}$. To offset variation in fabric dimension L_R along loading direction in the reference state, we define tensile strain $\epsilon = \frac{L_D - L_R}{L_R} \cdot 100\%$ to account for normalised extension $L_D - L_R$. We see good alignment between experiment and simulation, in terms of capturing the overall “J-shaped” curves (analogous to architected metamaterials [41] and biological fiber networks [42]) and the relative rigidity and extensibility of four knitted fabrics.

Uniaxial tensile test along warp direction demonstrates distinct two-stage regions of deformation to failure for all fabrics. Firstly, the jersey fabric, having consistent loop contacts throughout the fabric and hence possessing the simplest geometry, behaved most rigidly among the four fabrics studied during the first stage characterised by low linear stiffness (regime 1) at the magnitude of 0.1 MPa up to 30 % strain. Previous experimental study reported observation of geometry reconfiguration as yarns slide through loop contacts and straighten to align more towards applied tensile load [43], and our study provides quantitative evidences for such yarn dynamics that are summarised in Section 3.3. After that, the jersey fabric transitioned to a stage where the stiffness monotonically increased by up to 10 times (regime 2), during when stretching of individual yarns become noticeable and statistical measurements are discussed in Section 3.3. Secondly, we observe the garter fabric being the initially softest and most stretchable among the four fabrics studied, as it first undergoing a nearly linear region with the lowest slope (regime 1) at the magnitude of 0.01 MPa up to the largest strain magnitude of 60 %, followed by yarn stretching (regime 2) at a distinctively higher slope at the magnitude of 1 MPa in the data up to failure strain close to 90 %. On the other hand, the rib fabric being initially the most rigid and least extensible (excluding jersey), it first underwent yarn alignment with a slope almost two times higher than that for the garter fabric (regime 1), and only up to 40 % strain, comparably quickly followed by yarn stretching (regime 2) characterised by a much higher slope in the data up to failure at only 60 % strain. In addition, the seed fabric sustained the former loading stage (regime 1) with stiffness similar to that of

the rib fabric up to 50 % strain, and transitioned to the latter loading stage (regime 2) with stiffness reaching the asymptotic magnitude of 1 MPa.

We observe similar transition behaviour upon uniaxial loading along weft direction, as all fabrics are initially soft and stretchable, followed by strain hardening as geometric flexibility from the mesoscale patterns are exhausted. However, the relative rigidity and extensibility of fabrics are now different. Though the jersey fabric is again the most rigid and undertook strain-hardening the soonest at 30 % strain during loading regime 1, the relative variation in stiffness among the four fabrics during this loading regime is negligible. The rib fabric, previously representative of rigid behaviour under tension along warp direction, now becomes the initially softest and most stretchable under tension along weft direction, as it first undergoing yarn alignment of a (regime 1) at almost negligible magnitude up to more than 100 % strain, followed by yarn stretching (regime 2) at a noticeably higher slope at the magnitude of 0.1 MPa in the data up to failure strain more than 150 %. On the other hand, the garter fabric under tension along weft direction changes to be the initially most rigid and least extensible (excluding jersey), as it first underwent yarn alignment with a slope almost two times higher than that for the rib fabric (regime 1), and only up to 50 % strain, comparably quickly followed by yarn stretching (regime 2) characterised by a much higher slope approaching the magnitude of 1 MPa in the data up to failure at only close to 100 % strain. In addition, the seed fabric undertook mechanical behaviour close to that of the garter fabric.

It is well accepted that the precise matching between reduced-order constitutive models and experimental tests on knitted fabric is challenging [34, 24, 28, 27, 29, 30]. Though our simulation model recovers the general two-stage nonlinear elastic behaviour and the relative responses among the four basic weft-knitted fabrics well, we notice the limitation of our model, particularly when modelling the behaviour as fabrics transition to the stretching-dominant stage. This mainly comes from the limitation of our assumption on linear elasticity. We further discuss this limitation in Section 3.3, as statistical measurements on stretch of individual yarn segment for all studied fabrics and loading conditions are collected.

3.3. Mechanical role of yarn dynamics on fabric extensibility and anisotropy

To probe into how yarn rearrangements influence the macroscopic extensibility of knitted fabrics, we measured the projection of individual yarn segments on to the loading direction of warp in Fig. 6 and of weft Fig. 7.

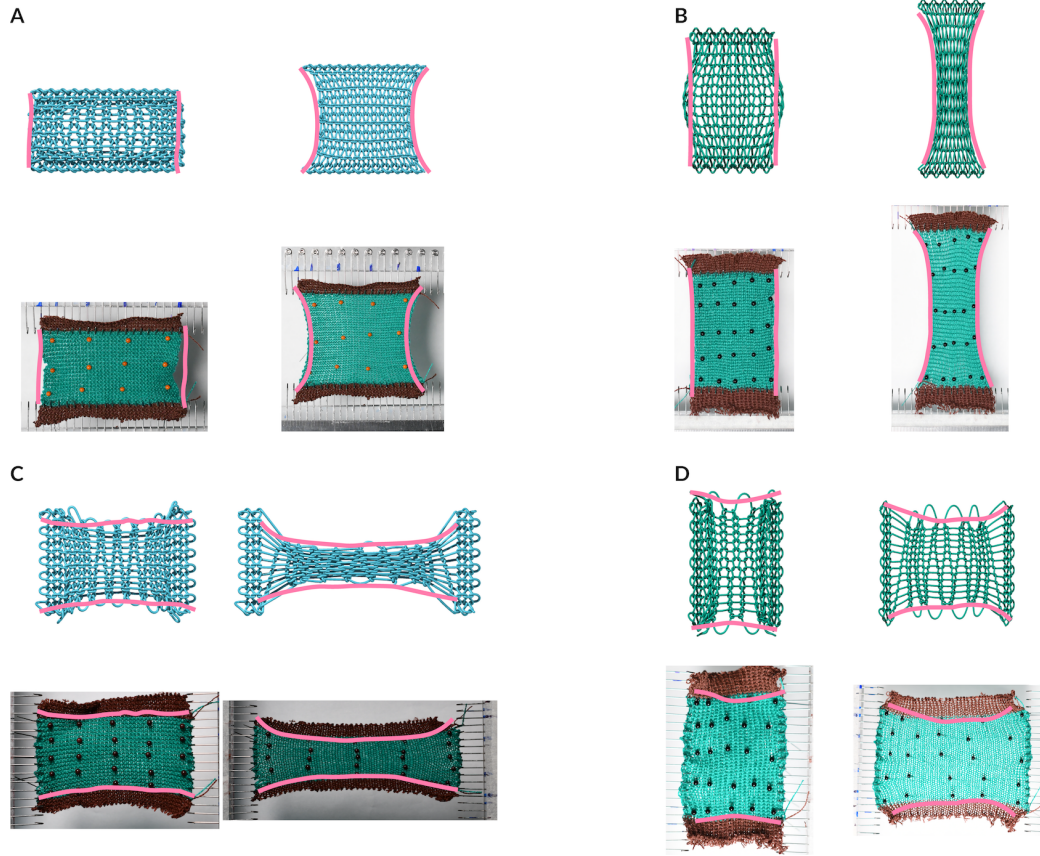


Figure 5: Deformation profiles from simulation (top) and experiment (bottom) at SI20% strain and 80 % strain respectively for (A) garter 1 by 1 when subjected to uniaxial tension along warp direction, (B) rib 1 by 1 when subjected to uniaxial tension along warp direction, (C) garter 1 by 1 when subjected to uniaxial tension along weft direction, (D) rib 1 by 1 when subjected to uniaxial tension along weft direction. Note that free ends of the fabrics with the same pattern and loading condition are marked with the same curves to provide a visual comparison between simulation and experiment on the deformation profiles.

With an angular increment (bin size) of 5 degrees, we can track the overall evolution of yarn segments as they align closer with the applied load as tensile strain increased from 0 % to 120 %. This quantitative evidence compliments experimental observation of reorientation of yarn segments to exploit geometric degrees of freedom within the network of connected yarn segments. Such geometric rearrangement of yarn segments rather than material stretching of yarn segments contributed to the compliant behaviour during the initial stage of fabric mechanical response. Statistical distributions of yarn segment stretch in Fig. 8 and Fig. 9 further support the yarn reorientation mechanism during the initial loading on fabrics, as distribution peaks remain within the range for negligible segment stretch while fabrics are stretched until transitions occur. It is worth noticing that even as fabrics transition to higher strain range (close to or more than 100 %) and yarn segments that are most stretched to almost 20 %, these segments account for less than 20 % of all yarn segments. Therefore, it is reasonable to assume linear elasticity to measure the averaged macroscopic behaviour of fabrics, despite quantitative evidence for such inhomogeneous mechanical field of segment stretch.

Previously we also observed anisotropy from knitted fabrics, which is topology-dependent. Taking the most representative examples as garter and rib, the former has a softer mechanical response and sustains a higher elastic strain range when subjected to tension along fabric warp direction rather than weft direction. On the contrary, the latter behaves in a stiffer manner within a lower elastic strain range when responding to tension along fabric weft direction rather than warp direction. To probe into the influence of fabric structure on anisotropy, we start from examining their geometric configurations in reference state, with reference to Fig. 6 and Fig. 7. The garter fabric initially has less than 10 % of yarn segments aligning with the warp direction within a difference of 10 degrees, but has more than 20 % similarly close yarn alignment with the weft direction. On the other hand, the rib fabric has more than 20 % of yarn segments aligning similarly close to the warp direction, but just less than 15 % yarn alignment with the weft direction in reference state. The lower frequency of close yarn alignment with the loading direction, the more geometric degrees of freedom to exploit when yarn segments rearrange themselves to manifest applied stress within the hierarchical system, leading to the fabric behaving more compliantly under this loading direction rather than the orthogonal loading direction. Moreover, if we examine Fig. 8 and Fig. 9, we see that for a fabric to behave relatively softer and more compliant under a fixed loading condition, the shift of its

distribution peak of yarn segment stretch takes place slower towards a higher stretch range, with fixed steps to stretch the fabric.

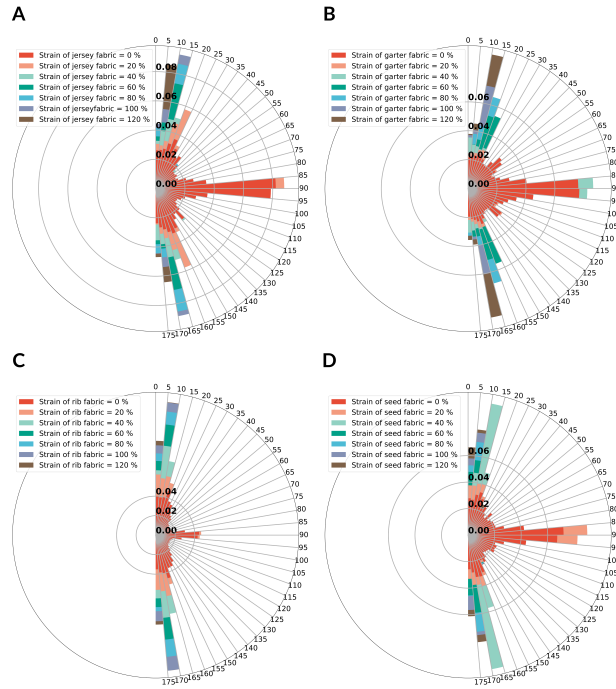


Figure 6: Rose diagram measuring the alignment of segment with respect to the loading direction for all samples (A) jersey, (B) garter 1 by 1, (C) rib 1 by 1 and (D) seed 1 by 1 under uniaxial tension along warp direction.

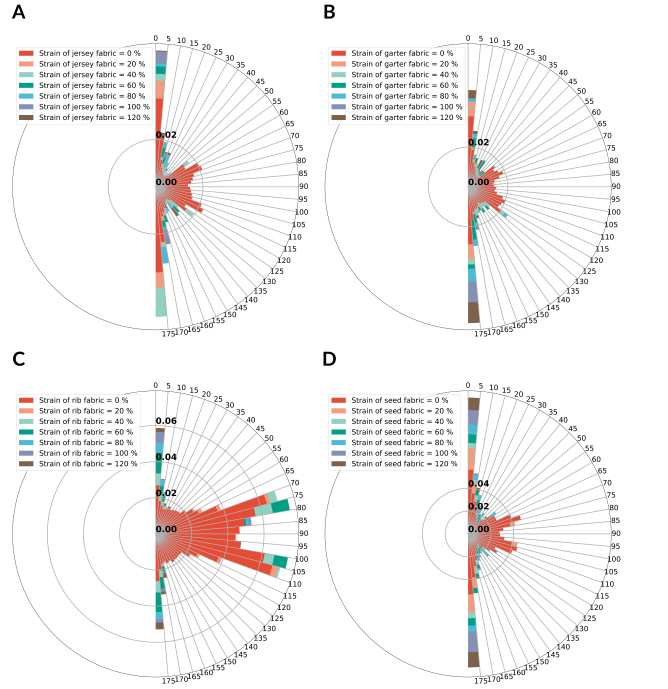


Figure 7: Rose diagram measuring the alignment of segment with respect to the loading direction for all samples (A) jersey, (B) garter 1 by 1, (C) rib 1 by 1 and (D) seed 1 by 1 under uniaxial tension along weft direction.

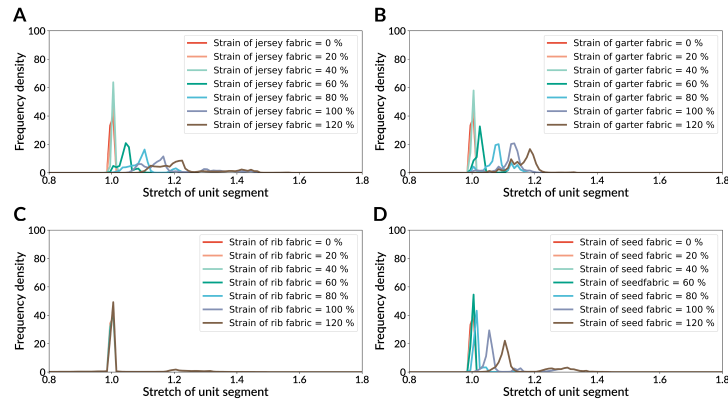


Figure 8: Histogram measuring the stretch segment for all samples (A) jersey, (B) garter 1 by 1, (C) rib 1 by 1 and (D) seed 1 by 1 under uniaxial tension along warp direction.

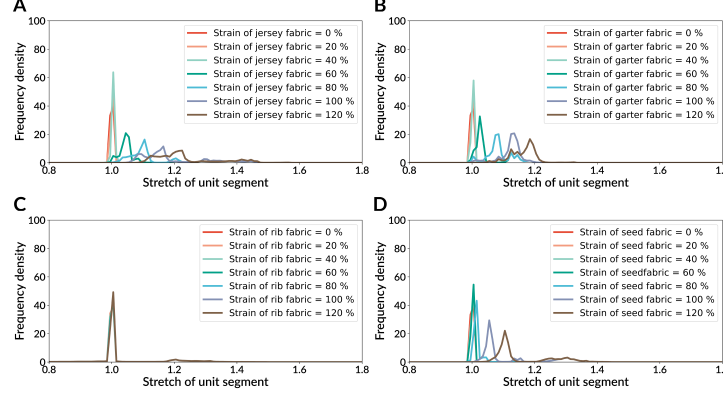


Figure 9: Histogram measuring the stretch segment for all samples (A) jersey, (B) garter 1 by 1, (C) rib 1 by 1 and (D) seed 1 by 1 under uniaxial tension along weft direction.

3.4. Demonstration of the design space

Here we present a gallery of multi-structure knitted fabrics with varying spatial distributions: (A) half garter 1 by 1 placed on top and half jersey placed on bottom; (B) half garter 1 by 1 placed in the middle and quarter jersey placed on both ends; (C) half rib 1 by 1 placed on top and half jersey placed on bottom (Fig. 10). We demonstrate their mechanical responses to uniaxial tension at fixed steps of uniaxial tensile strain. Utilising the distinctive mechanical properties of structures discussed in Sec. 3.2, we designed asymmetric primitives, with (A) being soft and extensible and (C) being rigid and less extensible along the fabric warp direction. Moreover, even with the same volumetric composition, varying spatial distribution of structures (A and B) leads to expanded set of fabric configurations. These knitted fabrics can morph compliantly with different geometric configurations characterised by varying side profiles, showing potential application in custom fit for wearables. Moreover, the anisotropy of fabric structures make them versatile in multi-objective applications, such as soft robotics. Last but not least, the side space opened up while these knitted fabrics are stretched enables them to be implemented as responsive panels, an emerging class of architectural component.

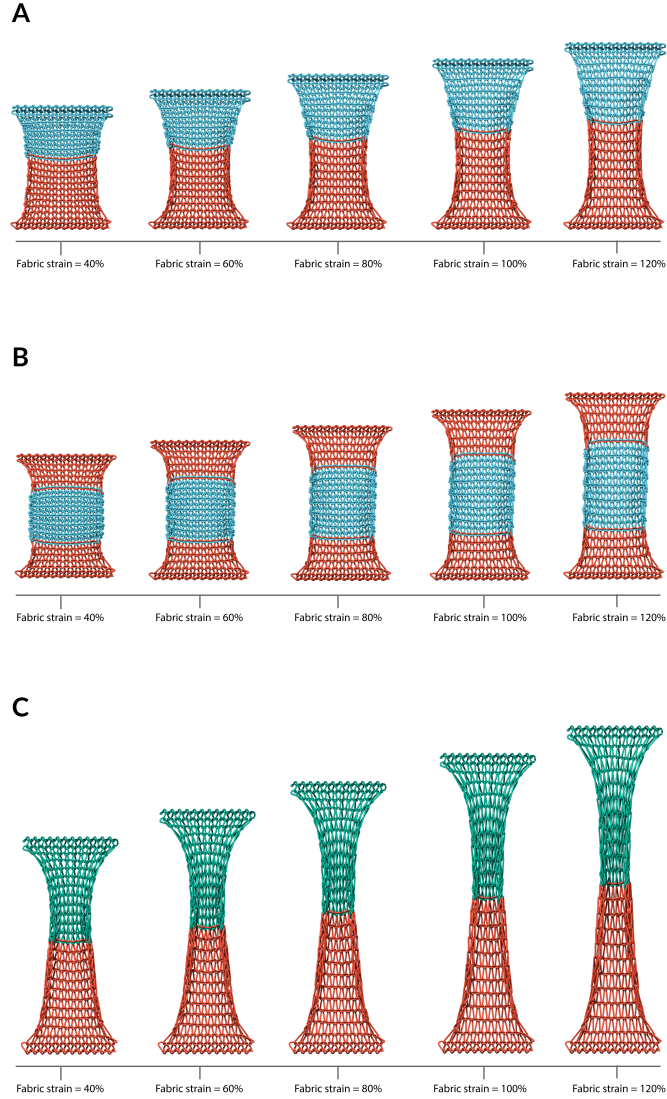


Figure 10: multi-structure knitted fabrics consisting of varying topology and spatial distributions (A) top half: garter 1 by 1, bottom half: jersey; (B) top quarter: jersey, middle half: garter 1 by 1, bottom quarter: jersey; (C) top half: garter 1 by 1, bottom half: jersey stretched with uniaxial tension along warp direction ranging from 40 % to 120 % strain.

4. Conclusion

We have presented a mechanics-centered computational model to simulate the large deformation of knitted fabrics at compatible scale to their emerging engineering applications as wearables and soft robotics. By defining a dynamic formulation of the governing equation, with constitutive law at each yarn segment defined, we have implemented an adaptive integration scheme that can efficiently solve for the evolution of such complex system with hierarchical geometric representation. Our numerical study complimented by experimental evidence show not only the fundamental nonlinear elastic response of knitted fabrics, noticeably characterised by two-stage behaviour analogous to fiber-based biological systems, polymer networks and architected materials with geometric degrees of freedom arising across-scale, but also the wide range of initial-stage stiffness and extensibility across fabrics with varying topology. Using this model, we can extract across-scale mechanisms to support the investigation of mechanical roles of yarn dynamics on fabric extensibility and anisotropy, with measurements of inhomogeneous mechanical quantities that are not feasible from experiments. Moreover, this model can be used to explore the enormous design space of knitted fabrics, as we exploit their topology-dependent mechanical properties through varying spatial distributions. By doing so, we hope to guide the mechanical programmability of knitted fabrics towards more engineering applications as functional textiles.

5. Implementation details of the numerical method

5.1. Numerical integration

The numerical simulations in this paper are performed using a custom C++ code that uses the OpenMP library [44] for multithreading. The core of the simulation involves integrating the ODE system for the position \mathbf{q}_k and velocity $\dot{\mathbf{q}}_k$ degrees of freedom described in Eqs. (2) & (3). This is solved using the fourth-order adaptive “first same as last” (FSAL) Runge–Kutta method [45]. This method uses five intermediate stages, where the first four can be used construct a fourth-order accurate solution, and the final stage can be used to construct an auxiliary third-order accurate solution for step size selection. With the FSAL property, the final stage can be re-used as the first stage of the next step, reducing the total computational work. We implement adaptive step size selection via the procedures described by Hairer et al. [45], which uses a combination of absolute tolerance $Atol$ and relative

tolerance $Rtol$. Initial step size selection is also performed using the methods of Hairer et al. [45].

Adaptive integration is beneficial for our simulations, since the appropriate step size choices vary greatly over the course of the simulation. In the initial stages, yarn elasticity is the most important physical effect and large timesteps can be taken. Once contact forces become important, the timestep sizes are substantially reduced. Similar methods have been employed in the simulation of crumpled sheets [46], which has comparable behavior.

Our simulations output snapshots at equally spaced time intervals. Since the timesteps are chosen adaptively, the integration time points will not align with the output time points in general. To solve this issue, we make use of dense output [45] and construct a cubic Hermite interpolant of the simulation state over each integration time step. Evaluating this interpolant at the output time point results in a fourth-order accurate approximation of the solution. The snapshots are outputted as binary files that contain the complete simulation state, which can be post-processed to perform a variety of analyses.

It is worth noting that the ODE system representing the yarn mechanics is not infinitely differentiable, since the contact forces are discretely switched on and off as yarns move past each other. Proving that the Runge–Kutta scheme is fourth-order accurate requires that the mathematical solution has Taylor expansions up to fourth order, which is not true in the case when an integration timestep passes over a moment when a contact force is switched on or off. Because of this, it is not possible to guarantee that the results are fourth-order accurate. Nevertheless, we opt to use the fourth-order scheme since it results in good accuracy and performance overall. Furthermore, Hairer et al. [45] demonstrate that in practical cases, adaptive-timestep integrators can approach high-order accuracy even when the ODE system lacks sufficient smoothness, since the integrator can automatically refine the timestep when passing over a discrete switch in the ODE, minimizing the additional error incurred.

5.2. Linear system

For a single yarn with N spline segments we write $\mathbf{q} \in \mathbb{R}^{3N+3}$ and $\dot{\mathbf{q}} \in \mathbb{R}^{3N+3}$ to be the vectors describing the yarn position and velocity, respectively. From Eqs. (6) & (8) the general equation of motion for a particular component

	$k = -1$	$k = 0$	$k = 1$	$k = 2$	$k = 3$	$k = 4$
$j = -1$	$1/252$	$43/1680$	$1/84$	$1/5040$		
$j = 0$	$43/1680$	$151/630$	$59/280$	$1/42$	$1/5040$	
$j = 1$	$1/84$	$59/280$	$599/1260$	$397/1680$	$1/42$	$1/5040$

Table 2: Coefficients in the matrix M , defined in Eq. (9) arising from the kinetic energy term in the Lagrangian formulation of the yarn dynamics.

$(\mathbf{q}_k, \dot{\mathbf{q}}_k)$ is given by

$$\frac{d}{dt}([M\dot{\mathbf{q}}]_k) = \left(\nabla_{\mathbf{q}_k} V(\mathbf{q}) + \nabla_{\dot{\mathbf{q}}_k} D(\mathbf{q}, \dot{\mathbf{q}}) \right), \quad (23)$$

$$\frac{d}{dt}(\mathbf{q}_k) = \dot{\mathbf{q}}_k \quad (24)$$

where M is a banded matrix whose components are defined by Eq. (9). For $2 \leq j \leq N - 2$, away from the end points, the components of M are given by

$$M_{jk} = \begin{cases} \frac{151}{315} & \text{if } k = j, \\ \frac{397}{1680} & \text{if } |k - j| = 1, \\ \frac{1}{42} & \text{if } |k - j| = 2, \\ \frac{1}{5040} & \text{if } |k - j| = 3, \\ 0 & \text{otherwise.} \end{cases} \quad (25)$$

Near the end points, the matrix values change, because the B-spline functions are no longer fully contained within Ω . The values for $j < 2$ are given in Table 2, and the values for $j > N - 2$ are obtained via symmetry. Our code can also handle the case when either the position or direction of the end point is fixed, which results in adjusting the linear system to incorporate a linear algebraic constraint.

To solve the ODE system in Eqs. (23) & (24) it is necessary to solve the linear system $Mq = f$ where $q \in \mathbb{R}^{(3N+3) \times 3}$ are entries of $\dot{\mathbf{q}}$ arranged into a matrix, with the x , y , and z components each in one column. $f \in \mathbb{R}^{(3N+3) \times 3}$ are the corresponding source terms, from the right hand side of Eq. (23). The matrix M remains fixed throughout the simulation, and therefore during the initialization its LU factorization is precomputed. This accelerates the solution of the linear system during the simulation. The LAPACK library is used, with the LU factorization being performed using the `dgbtrf` routine for a general banded matrix in double-precision floating point arithmetic. The `dgbtrs` routine is then used to solve the linear systems during the timesteps.

5.3. Contact sphere diameter calculations

As described in Sec. 2.3, yarn–yarn contact forces are handled by introducing n equally spaced spheres of radius d_{con} along each spline segment. If $d_{\text{con}} = d$, then the envelope formed by the spheres would be smaller than the yarn itself. We therefore systematically choose d_{con} to better approximate the yarn shape. Let $D = l/(2n)$ be the distance between successive contact spheres. Assuming that D is small relative to d , the contact sphere diameter is chosen to be

$$d_{\text{con}} = \frac{d + \sqrt{d^2 + \frac{2}{3}D^2}}{2}, \quad (26)$$

which ensures that the average diameter of the envelope of spheres is equal to d . To choose the number of contact spheres, we define a parameter α corresponding to the maximum allowable mean square deviation between the contact sphere envelope and the filament diameter, which is typically set to be several percent. Then the number of contact spheres satisfies

$$n = \left\lceil \frac{l}{d\sqrt{6(1+\alpha)\alpha}} \right\rceil, \quad (27)$$

where $\lceil \cdot \rceil$ is the ceiling operator. Since the contact spheres overlap, when considering Eq. (17), it is necessary to screen out the effect of interactions from neighboring spheres along the same yarn. This is done by defining a screening number $n_{\text{screen}} = \lceil \beta d_{\text{con}}/D \rceil$ where β is a dimensionless parameter. Terms in the sum of Eq. 17 are only considered if the indices of the spheres are separated by at least n_{screen} .

5.4. Tethering forces and initial sample generation

To perform the uniaxial tension tests, tethering forces are applied to the fabric to fix the displacement in two end regions. This procedure is similar to the approach used in the immersed boundary method [47] to simulate fixed walls [48]. Specifically, two regions D_+ and D_- are defined, where typically $D_{\pm} = \{(x, y, z) \in \mathbb{R}^3 : \pm y > y_{\text{fix}}\}$ for a constant y_{fix} when pulling a sample in the y direction.

During the simulation initialization, all spline segments that lie fully within D_+ and D_- are marked, and the reference position of each quadrature point within each marked segment is recorded. Using this information, the

additional energy contributions

$$V_{\pm}^t = k_t \int_{\Omega} I_{D_{\pm}}(s) \|\mathbf{y}(s) - \mathbf{F}_{\pm}(\mathbf{y}_{\text{ref}}(s), t)\|^2 ds \quad (28)$$

are added to Eq. (6), where $I_{D_{\pm}}(s)$ is equal to one in spline segments marked within D_{\pm} , and zero otherwise. Here, $\mathbf{F}_{\pm} : \mathbb{R}^3 \rightarrow \mathbb{R}^3$ are time-dependent affine transformations of the reference position. They can be used to apply the constant pulling velocity in the end regions. The forces that are measured in the tension tests are computed as the total force applied to the fabric in each tethered region.

As described in Sec. 6.5, the experimental samples created by the knitting machine are already under substantial tension, meaning that the yarns are much tighter than the examples shown in Figs. 1 & 2. It is difficult to initialize the simulation in tighter configurations directly, since any overlaps in the initial state may result in very large initial contact forces. Because of this, we perform a preliminary simulation to generate the samples for the tension tests. We initialize the yarn in a loose configuration given by Eq. (22), and then make the spline rest length l a function of time, applying a linear ramping so that

$$l(t) = \begin{cases} l_0 - (1 - \eta)\frac{t}{T_r} & \text{if } t < T_r, \\ \eta l_0 & \text{if } t \geq T_r, \end{cases} \quad (29)$$

where l_0 is the initial rest length of the yarn, T_r is the duration of the ramping, and η is a dimensionless ratio chosen to ensure that the final state matches the same compression as the experimental samples. During this procedure, the two end regions are tethered using the energy contributions in Eq. (28) to prevent the sample from curling. Since the rest length is reduced, the affine transformations \mathbf{F}_{\pm} are used to apply a commensurable shrinkage to the tethered regions. The precise amount of shrinkage is determined by comparing to the geometry of the experimental samples. After this preliminary simulation is performed, the yarn state is saved and then used as the starting configuration for the tension test simulations.

6. Materials and Experiments

6.1. Material selection

Commercially available acrylic spun yarns (16/2 Vybralite Acrylic Yarns, National Spinning Co. by Peter Patchis Yarns, USA) were selected to create

all knitted fabric swatches, which were mainly collected for the study of Sanchez et al. [43]. We performed the pull-out and bending tests on a single yarn, in order to benchmark the previously reported stretching stiffness, and to calibrate the bending stiffness of selected experimental material.

6.2. *Filament diameter*

Scanning Electron Microscope (SEM) images were taken with a Tescan Vega scanning electron microscope for the acrylic spun yarns, in order to measure the diameter of the yarn accurately. To adjust for camera orientation, we used Adobe Photoshop to calculate the projected area of the yarn segment under orthogonal projection and used that to calculate the effective yarn diameter as projected area divided by the fixed yarn length of 20 mm. This process was repeated three times on three different yarn segments from the same material. The averaged yarn diameter, 0.0524 cm, from experimental measurements was used to benchmark the yarn diameter used in simulation. In addition, we assume a circular and consistent cross section with this calibrated effective radius from onward for related calculations.

6.3. *Yarn linear density*

We adopt yarn linear density defined as

$$\rho = \frac{M}{l}, \quad (30)$$

which is a standard definition adopted in the textile industry and is provided by the manufacturer as 0.077 g/m. The equivalent term in simulation is 7.7×10^{-4} g/cm.

6.4. Characterisation of yarn properties

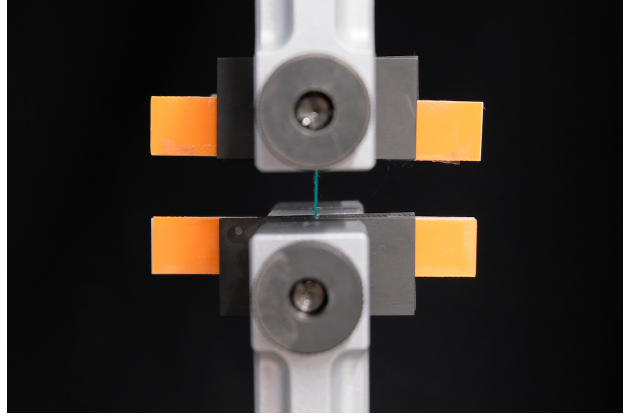


Figure 11: Pull-out test on a single yarn to characterize the stretching stiffness of a single yarn.

Figure 11 illustrates the experimental set up for a pull-out test on a single yarn, in order to measure its stretching stiffness. A pull-out test of a single yarn adhered to acrylic boards with instant adhesive to prevent slippage was performed on at least three different samples, with fixed gauge length recorded to calculate tensile strain. All samples were tested at a rate of 5 mm/min on a Universal Testing Machine (Instron 5566R), and tensile force F and tensile strain ϵ were directly measured during loading processes. The stretching stiffness of a single yarn

$$E^s = \frac{F}{\pi r^2 \epsilon} \quad (31)$$

first underwent a linear stage with 79.0 MPa within 5 % tensile strain, followed by softening behaviour. In all simulation tests, we assumed linear elasticity and calibrated the equivalent stretching stiffness to be $7.9 \times 10^8 \text{ g}/(\text{cm s}^2)$. This assumption was further testified by histogram measurement of the stretch of individual yarn segments. On average, less than 20 % yarn segments are stretched by more than 5 % even when the fabric samples are stretched by more than 60 %.

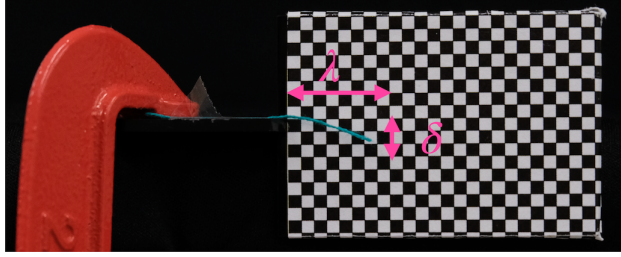


Figure 12: Bending test on a cantilevered single yarn to characterize the bending stiffness of a single yarn.

Figure 12 illustrates the experimental set up for a bending test on a single yarn cantilevered at one end with the free end consisting a horizontal length λ , and drops by a vertical displacement of δ due to gravity. We assume that gravity of the yarn acts as a distributed load $q = \pi r^2 \rho g$ and referring to Chakrabarti et al. [49], the bending stiffness of such soft material can be determined from sets of fixed λ and measured δ from:

$$E^b = \frac{q\lambda^4}{8\delta I}. \quad (32)$$

For each bending test, we took high resolution photos of the cantilevered yarn segment, with pixel images on the background. Each pixel grid represents 0.25 mm and post processing in Adobe Photoshop was done to ensure an orthogonal perspective. From a series of bending tests on three different yarn segments, we calibrated the bending stiffness of the used acrylic spun yarn to be 0.249 MPa and its equivalent parameter in simulation is $2.49 \times 10^4 \text{ g}/(\text{cm s}^2)$. Note that the measured bending stiffness differs from the stretching stiffness by several magnitudes due to the soft nature of used material.

6.5. Fabrication of knitted fabrics

For reference we summarise the experimental protocol to fabricate and to test the fabric swatches from Sanchez et al. [43] here. In total, six samples for each knitted structure (jersey, garter 1 by 1, rib 1 by 1 and seed 1 by 1) were fabricated with the same settings on stitch spacing and machine tension on a Kniterate V-bed knitting machine S8 (Kniterate, EU), and all consisting of 41 wales by 40 courses (i.e., number of stitches along the warp and the weft directions respectively). The “knitout” programme [50] was used to convert the Python frontend (specified by McCann et al. [51]) to Kniterate-specific

machine language “kcode”, in order to operate the knitting machine. The unit arclength of each fabric l was determined by

$$L = \frac{M}{\rho N_w N_c}, \quad (33)$$

from directly measured mass of fabricated sample M , fixed yarn linear density from the manufacturer and number of wales N_w and number of courses N_c . After fabrication, all samples were left at ambient conditions for 24-48 hours to enable material relaxation, as responding to residual stresses from the manufacturing process. Then, the dimensions of all samples were measured and approximated as those of samples in their reference states.

6.6. *Uniaxial tensile tests to characterise the knitted fabrics*

All knitted fabric samples were cyclically tested using Universal Testing Machiens (an Instron 5544A with a smaller-range load cell and an Instron 5566R with a larger-range load cell). The gauge lengths were recorded, in order to offset mismatch between previously recorded sample dimensions and ground-truth sample dimensions in stress-free states on the testing machines. These samples were pre-cycled to force magnitude of 20 N at a fixed rate of 10 mm/min during loading stage and 20 mm/min during unloading, followed by two cycles at a rate of 5 mm/min until reaching 15 N. This upper bound on force was selected empirically, in order to prevent fabrics from plastic deformation. For our study, we selected the mechanical responses measured after pre-cycling, as they were robustly repeated through cycles for the same fabric and the same tensile loading direction. Note that the strain ranges from experiments were smaller than those from numerics presented in this study, since the former were collected from a particular cycle of the cyclic tests way before failure.

Acknowledgment

This research was primarily supported by NSF through the Harvard University Materials Research Science and Engineering Center DMR-2011754.

Author Contribution

C.H.R. and K.B. designed the research and supervised the project. X.D. and C.H.R. carried out analytical derivations and coded the numerical model. X.D. and V.S. designed and conducted experiments. X.D. performed data analysis on raw experimental data and validation of numerical model from experimental data. X.D. and C.H.R. wrote the manuscript with input from all authors.

References

- [1] Samuel Poincloux, Mokhtar Adda-Bedia, and Frédéric Lechenault. Crackling dynamics in the mechanical response of knitted fabrics. *Physical Review Letters*, 121, 7 2018.
- [2] Samuel Poincloux, Mokhtar Adda-Bedia, and Frédéric Lechenault. Geometry and elasticity of a knitted fabric. *Physical Review X*, 8, 6 2018.
- [3] Fionnuala Connolly, Diana A. Wagner, Conor J. Walsh, and Katia Bertoldi. Sew-free anisotropic textile composites for rapid design and manufacturing of soft wearable robots. *Extreme Mechanics Letters*, 27:52–58, 2 2019.
- [4] Vanessa Sanchez, Conor J. Walsh, and Robert J. Wood. Textile technology for soft robotic and autonomous garments. *Advanced Functional Materials*, 31, 2 2021.
- [5] Lea Albaugh, Lining Yao, and Scott Hudson. Digital fabrication of soft actuated objects by machine knitting. pages 1–4, 2019.
- [6] Panagiotis Polygerinos, Zheng Wang, Kevin C Galloway, Robert J Wood, and Conor J Walsh. Soft robotic glove for combined assistance and at-home rehabilitation. *Robotics and Autonomous Systems*, pages 135–143, 2015.
- [7] Rachael Granberry, Kevin Eschen, Brad Holschuh, and Julianna Abel. Functionally graded knitted actuators with niti-based shape memory alloys for topographically self-fitting wearables. *Advanced Materials Technologies*, 4, 11 2019.
- [8] Irmandy Wicaksono, Carson Tucker, Tao Sun, Cesar Guerrero, Clare Liu, Wesley Woo, Eric Pence, and Canan Dagdeviren. A tailored, electronic textile conformable suit for large-scale spatiotemporal physiological sensing in vivo. *npj Flexible Electronics*, 4:5, 04 2020.
- [9] Yiyue Luo, Kui Wu, Andrew Spielberg, Michael Foshey, Daniela Rus, Tomás Palacios, and Wojciech Matusik. Digital fabrication of pneumatic actuators with integrated sensing by machine knitting. Association for Computing Machinery, 4 2022.

- [10] Min-Woo Han and Sung-Hoon Ahn. Blooming knit flowers: Loop-linked soft morphing structures for soft robotics. *Advanced Materials*, 29(13):1606580, 2017.
- [11] Yiyue Luo, Yunzhu Li, Pratyusha Sharma, Wan Shou, Kui Wu, Michael Foshey, Beichen Li, Tomás Palacios, Antonio Torralba, and Wojciech Matusik. Learning human–environment interactions using conformal tactile textiles. *Nature Electronics*, 4:193–201, 2021.
- [12] Irmandy Wicaksono and Joseph A Paradiso. Fabrickeyboard: multimodal textile sensate media as an expressive and deformable musical interface. *New Interfaces for Musical Expression*, 17:348–353, 2017.
- [13] Zeguang Pei, Xiangzhang Xiong, Jian He, and Yan Zhang. Highly stretchable and durable conductive knitted fabrics for the skins of soft robots. *Soft Robotics*, 6:687–700, 12 2019.
- [14] F.T. Peirce. Geometrical principles applicable to the design of functional fabrics. *Textile Research Journal*, 17(3):123–147, 1947.
- [15] G. A. V. Leaf and A. Glaskin. 43—the geometry of a plain knitted loop. *Journal of the Textile Institute Transactions*, 46(9):T587–T605, 1955.
- [16] D. L. Munden. 26—the geometry and dimensional properties of plain-knit fabrics. *Journal of the Textile Institute Transactions*, 50(7):T448–T471, 1959.
- [17] Miklós Bergou, Max Wardetzky, Stephen Robinson, and Basile Audoly. Discrete elastic rods. *ACM Transactions on Graphics*, 21:1–12, 2008.
- [18] Jonathan M. Kaldor, Doug L. James, and Steve Marschner. Simulating knitted cloth at the yarn level. *ACM Transactions on Graphics*, 27:1–9, 8 2008.
- [19] Gabriel Cirio, Jorge Lopez-Moreno, David Miraut, and Miguel A. Otaduy. Yarn-level simulation of woven cloth. *ACM Transactions on Graphics*, 33, 11 2014.
- [20] Jonathan Leaf, Rundong Wu, Eston Schweickart, Doug L. James, and Steve Marschner. Interactive design of periodic yarn-level cloth patterns. *ACM Transactions on Graphics*, 37:1–15, 12 2018.

- [21] Demetri Terzopoulos, John Platt, Alan Barr, and Kurt Fleischert. Elastically deformable models. *ACM SIGGRAPH Computer Graphics*, 21:205–214, 1987.
- [22] David Baraff and Andrew Witkin. Large steps in cloth simulation. 1998.
- [23] David E. Breen, Donald H. House, and Michael J. Wozny. Predicting the drape of woven cloth using interacting particles. In *Proceedings of the 21st Annual Conference on Computer Graphics and Interactive Techniques*, SIGGRAPH '94, page 365–372, New York, NY, USA, 1994. Association for Computing Machinery.
- [24] Mark S. Yeoman, Daya Reddy, Hellmut C. Bowles, Deon Bezuidenhout, Peter Zilla, and Thomas Franz. A constitutive model for the warp-weft coupled non-linear behavior of knitted biomedical textiles. *Biomaterials*, 31:8484–8493, 11 2010.
- [25] Rahul F Narain Armin Samii James O, Images copyright Rahul Narain, Armin Samii, and James F O. Adaptive anisotropic remeshing for cloth simulation. *ACM Transactions on Graphics*, 31:1–10, 2012.
- [26] Cem Yuksel, Jonathan M Kaldor, Doug L James, and Steve Marschner. Stitch meshes for modeling knitted clothing with yarn-level detail. *ACM Transactions on Graphics*, 31:1–12, 2012.
- [27] Dani Liu, Daniel Christe, Bahareh Shakibajahromi, Chelsea Knittel, Nestor Castaneda, David Breen, Genevieve Dion, and Antonios Kotsos. On the role of material architecture in the mechanical behavior of knitted textiles. *International Journal of Solids and Structures*, 109:101–111, 2017.
- [28] T.D. Dinh, O. Weeger, S. Kaijima, and S.-K. Yeung. Prediction of mechanical properties of knitted fabrics under tensile and shear loading: Mesoscale analysis using representative unit cells and its validation. *Composites Part B: Engineering*, 148:81–92, 2018.
- [29] Oliver Weeger, Amir Hosein Sakhaei, Ying Yi Tan, Yu Han Quek, Tat Lin Lee, Sai Kit Yeung, Sawako Kaijima, and Martin L. Dunn. Nonlinear multi-scale modelling, simulation and validation of 3d knitted textiles. *Applied Composite Materials*, 25:797–810, 8 2018.

- [30] Liwei Wu, Feng Zhao, Junbo Xie, Xianyan Wu, Qian Jiang, and Jia-Horng Lin. The deformation behaviors and mechanism of weft knitted fabric based on micro-scale virtual fiber model. *International Journal of Mechanical Sciences*, 187:105929, 2020.
- [31] Georg Sperl, Rahul Narain, and Chris Wojtan. Mechanics-aware deformation of yarn pattern geometry. *ACM Transactions on Graphics*, 40:1–11, 7 2021.
- [32] Shashank G Markande and Elisabetta A Matsumoto. Knotty knits are tangles on tori, 2020.
- [33] Endre Süli and David F. Mayers. *An Introduction to Numerical Analysis*. Cambridge University Press, 2003.
- [34] Savvas Vassiliadis, Argyro Kallivretaki, and Christopher Provatidis. Mechanical simulation of the plain weft knitted fabrics. *International Journal of Clothing Science and Technology*, 19:109–130, 03 2007.
- [35] K H Leong, S Ramakrishna, Z M Huang, and G A Bibo. The potential of knitting for engineering composites-a review. *Composites A*, 2000.
- [36] D. J Spencer. *Knitting Technology - A Comprehensive Handbook and Practical Guide (3rd Edition)*. Woodhead Publishing Series in Textiles. Woodhead Publishing, Cambridge, 2001.
- [37] Emmanuel Piuze, Paul G. Kry, and Kaleem Siddiqi. Generalized helioids for modeling hair geometry. volume 30, pages 247–256. Blackwell Publishing Ltd, 2011.
- [38] Paras Wadekar, Prateek Goel, Chelsea Amanatides, Genevieve Dion, Randall D. Kamien, and David E. Breen. Geometric modeling of knitted fabrics using helicoid scaffolds. *Journal of Engineered Fibers and Fabrics*, 15, 2020.
- [39] L. Dagum and R. Menon. Openmp: an industry standard api for shared-memory programming. *IEEE Computational Science and Engineering*, 5(1):46–55, 1998.
- [40] Eman Abd Elzaher Eltahan, Mohamed Sultan, and Abou Bakr Mito. Determination of loop length, tightness factor and porosity of single

- jersey knitted fabric. *Alexandria Engineering Journal*, 55:851–856, 6 2016.
- [41] Widiyanto P. Moestopo, Sammy Shaker, Weiting Deng, and Julia R. Greer. Knots are not for naught: Design, properties, and topology of hierarchical intertwined microarchitected materials. *Science Advances*, 9(10):eade6725, 2023.
 - [42] Y.C. Fung. *Biomechanics: mechanical properties of living tissues*. 1996.
 - [43] Vanessa Sanchez, Kausalya Mahadevan, Gabrielle Ohlson, Moritz A. Graule, Michelle C. Yuen, Clark B. Teeple, James C. Weaver, James McCann, Katia Bertoldi, and Robert J. Wood. 3d knitting for pneumatic soft robotics. *Advanced Functional Materials*, n/a(n/a):2212541, 2023.
 - [44] L. Dagum and R. Menon. OpenMP: an industry standard API for shared-memory programming. *IEEE Computational Science and Engineering*, 5(1):46–55, 1998.
 - [45] E. Hairer, S. P. Nørsett, and G. Wanner. *Solving Ordinary Differential Equations I: Nonstiff Problems*. Springer, Berlin, 1993.
 - [46] Jovana Andrejevic and Chris H. Rycroft. Simulation of crumpled sheets via alternating quasistatic and dynamic representations. *Journal of Computational Physics*, 471:111607, 2022.
 - [47] Charles S. Peskin. The immersed boundary method. *Acta Numerica*, 11:479–517, 1 2002.
 - [48] Thomas G. Fai and Chris H. Rycroft. Lubricated immersed boundary method in two dimensions. *Journal of Computational Physics*, 356:319–339, 2018.
 - [49] Aditi Chakrabarti, Salem Al-Mosleh, and L. Mahadevan. Instabilities and patterns in a submerged jelling jet. *Soft Matter*, 17:9745–9754, 11 2021.
 - [50] James McCann. The ”knitout” program, 2017.
 - [51] James McCann, Lea Albaugh, Vidya Narayanan, April Grow, Wojciech Matusik, Jennifer Mankoff, and Jessica Hodgins. A compiler for 3d machine knitting. *ACM Trans. Graph.*, 35(4), jul 2016.